European Biophysics Journal (2025) 54:295–303
https://doi.org/10.1007/s00249-025-01759-7

ORIGINAL ARTICLE

Predictive model for evolving density and viscosity gradients in band-forming ultracentrifugation

Lukas Dobler[1] · Emre Brookes[2] · Piotr Grodzki[3] · Maciej Lisicki[3] · Borries Demeler[2,4] · Helmut Cölfen[1] · Piotr Szymczak[3]

Received: 26 March 2025 / Revised: 24 April 2025 / Accepted: 13 May 2025 / Published online: 13 June 2025

Abstract

Band-forming experiments allow the study of a wide variety of systems by overlaying two solutions with different densities in an analytical ultracentrifuge. Despite their potential benefits over other methods, these experiments are rarely used because all available fitting software encounters systematic errors, failing to account for the evolving gradient in density and viscosity due to diffusive mixing between the two layers. We develop and experimentally validate a predictive model for the purely diffusive mixing of two solutions in a cylindrical system. Capturing the space- and time-dependent evolution of density and viscosity in band-forming experiments, the model enhances their interpretation and underscores the need for analysis software to account for these dynamic changes.

Keywords Analytical ultracentrifugation · Band-forming · Dynamic gradient · Solvent properties · Diffusion · Solvent mixing

Introduction

Analytical ultracentrifugation (AUC) is a first-principles experimental technique that is used to characterize nanoscale molecules in the solution state by recording their sedimentation profiles. It has been applied to a wide range of systems, including proteins (Edwards et al. 2020; Chaton and Herr 2015), viruses (Maruno et al. 2021; Wawra et al. 2023; Sternisha et al. 2023; Khasa et al. 2021), nucleic acids (Edwards et al. 2020; Ranasinghe et al. 2023; Urban et al. 2016) and polymers (Planken and Cölfen 2010; Diaz et al. 2015), as well as nanoparticles composed of metals (Völkle et al. 2015; Schneider and Cölfen 2019, 2020; Wawra et al. 2018; Thajudeen et al. 2017; Lopez et al. 2022; González-Rubio et al. 2021; Urban et al. 2016), semiconductors (Börger et al. 2000; Walter et al. 2017; Karabudak et al. 2016), insulators (Goertz et al. 2009; Mittal et al. 2010; Uttinger et al. 2020) or lipids (Zhao et al. 2024; Henrickson et al. 2021). Its versatility relies on the use of different detectors, with the two most popular types being multiwavelength (MWL) UV/Vis absorbance detectors (Karabudak et al. 2016; Pearson et al. 2018), and Rayleigh interference detectors (Schilling and Krause 2015). The MWL-detection allows one to study complex mixtures and distinguish species not only by sedimentation but also by their spectral properties, making

✉ Piotr Szymczak
piotrek@fuw.edu.pl

Lukas Dobler
lukas.dobler@uni-konstanz.de

Emre Brookes
emre.brookes@umontana.edu

Piotr Grodzki
p.grodzki2@student.uw.edu.pl

Maciej Lisicki
Maciej.Lisicki@fuw.edu.pl

Borries Demeler
demeler@gmail.com

Helmut Cölfen
helmut.coelfen@uni-konstanz.de

[1] Department of Chemistry, Universität Konstanz, Konstanz, Germany

[2] Department of Chemistry and Biochemistry, University of Montana, Missoula, USA

[3] Institute of Theoretical Physics, Faculty of Physics, University of Warsaw, Warsaw, Poland

[4] Department of Chemistry and Biochemistry, University of Lethbridge, Lethbridge, Canada

it practical for biological and chemical samples (Maruno et al. 2021; Sternisha et al. 2023; Wawra et al. 2018; Lopez et al. 2022; Schneider and Cölfen 2019; Wawra et al. 2019; Henrickson et al. 2021; Karabudak et al. 2016; Völkle et al. 2015). In the past, various other detectors, such as Schlieren or fluorescence detectors, were commercially available and are still occasionally used (MacGregor et al. 2004; Wawra et al. 2019; Mächtle 1992, 1999; Xu and Cölfen 2021; Cölfen 2023). Although the most popular measurement mode is the traditional boundary experiment, often referred to as sedimentation velocity (SV) (Cölfen 2023), the capabilities of AUC are further extended by alternative experimental modes, such as speed ramp or density variation experiments.

An attractive alternative to traditional AUC techniques is the band-forming experiment (BFE). In contrast to a traditional setup, where the solute is initially uniformly distributed throughout the AUC cell at the beginning of the experiment, in a BFE the sample layer is placed on the top (closer to the axis of rotation) of the higher-density solution in the channel and subsequently centrifuged. BFE was first introduced by Vinograd et al. (1963) and requires the so-called Vinograd centerpieces, which are adapted by adding a reservoir near the top of the centerpiece channel. This reservoir is connected by a thin capillary to the solution channel. Upon commencement of centrifugation, the solution in the reservoir is transferred into the channel by centrifugal forces. To facilitate band formation, the solvent in the centerpiece channel must have a density higher than that of the solvent in the reservoir. Typically this density difference is created by (partially) replacing H_2O in the channel solution with D_2O. This creates a stacking effect and leads to the formation of a sharp band (Vinograd et al. 1963; Vinograd and Bruner 1966a, b). A sharp Gaussian peak is then formed for a homogeneous sample; as it migrates away from the meniscus, it broadens as a result of diffusion, just like the sigmoidal boundary in a traditional SV experiment.

BFEs offer a convenient way to investigate particle mixtures, chemical reactions, or biological systems *in-situ*. Typically, the solution in the reservoir is up to ten times more concentrated but has a volume smaller by a factor of 40, resulting in less sample consumption compared to traditional sedimentation boundary experiments. A common application of BFE is active enzyme centrifugation, in which an enzyme solution is overlaid onto the substrate solution (Chou et al. 2011). The enzyme can be investigated in its active state without purification (Chou et al. 2011). For non-biological samples, BFE can freeze products of chemical reactions, for example, the early stages of nucleation of nanoparticles, by sedimentation away from the phase boundary. This allows one to physical separate different species or generations of particles. This separation capability is crucial for observing reaction progress and isolating specific phases without the interference of transient dynamics, that could affect sample integrity during experiments involving nanoparticles (Börger et al. 2000; Karabudak et al. 2016; Schneider and Cölfen 2019, 2020). By combining the advantages of BFE with powerful detectors such as UV/Vis-MWL absorption, subnanometer size resolution becomes possible, as demonstrated for metal (Völkle et al. 2015) and semiconductor (Karabudak et al. 2016) nanoparticles.

Schneider and Cölfen (2018) and Schneider et al. (2018) demonstrated that mixing the upper phase with the lower phase in BFE leads to the formation of gradients in both viscosity and density. While the latter is a critical necessary element in achieving stable band sedimentation (Vinograd et al. 1963; Vinograd and Bruner 1966a, b), it had been neglected in all prior analyses. Due to the differences in density and viscosity between light and heavy water, the apparent sedimentation and diffusion coefficients of an analyte change over time and spatial position until diffusion equilibrium is reached, with the concentrations of light and heavy water becoming uniform throughout the channel. While there are density gradient experiments in the AUC utilizing co-sedimenting additives, like CsCl and Nycodenz, their analysis relies on data obtained when the system reaches equilibrium (Vinograd et al. 1963; Sternisha et al. 2023; Planken and Cölfen 2010). Furthermore, the experiment is only capable of determining the sample buoyant density, but not the sedimentation coefficient (Savelyev et al. 2023). In contrast, the BFE data is recorded when the system is out of equilibrium, with the gradient evolving over time due to D_2O - H_2O diffusion. Sedimentation transport can be neglected because the centrifugal force is not sufficient to sediment H_2O molecules in D_2O over the time span of the experiment. The time- and position-dependent changes of the solvent density and viscosity are not considered in common analysis software such as *sedfit* (Schuck 2000) and *UltraScan III* (Demeler and Gorbet 2016), which assume constant viscosity and density, and result in non-random and elevated residuals during data analysis. Recent studies utilizing BFE have simultaneously highlighted its advantages and limitations, leveraging its low sample consumption and high separational power to analyze adeno-associated virus vectors (Khasa et al. 2021; Maruno et al. 2023). The differences in sedimentation coefficients between SV-AUC and BFE-AUC reported by Maruno et al. highlight the challenges BFE data pose for standard analysis software. Gradient in viscosity and density can lead to artificial peak broadening, which may be misinterpreted as additional species.

While the problem of dynamic gradients was identified earlier (Schneider and Cölfen 2018; Schneider et al. 2018), no model has been proposed to accurately simulate the changes in density and viscosity. This lack of a theoretical description has hindered further investigation into how BFEs are influenced by these evolving gradients.

In this paper, we present a mathematical model for the evolution of dynamic gradients in density and viscosity to aid in the analysis of BFE data using Lamm equation modeling. The theoretical framework is based on the diffusion-driven mixing of light and heavy water. We validate the model predictions with recorded experimental data and numerical calculations to highlight the pronounced effect of cell geometry on viscosity and density gradients.

Experimental section

Materials

H_2O was sourced from a Milli-Q Synthesis A10 system, which was equipped with a Quantum EX Ultrapure Organex cartridge (Millipore). Deuterium oxide (D_2O) was obtained from Sigma Aldrich and used without any further purification steps.

Data acquisition

The sample, H_2O, was measured in a charcoal-filled Epon band-forming centerpiece with a 12 mm path length, purchased from Beckman. This has a small reservoir that holds up to a volume of 15 µL. The reservoir is connected to the sample channel through a narrow capillary. The centerpiece was scanned and a channel angle of 2.5° was determined.

The experiment was performed by overlaying H_2O over D_2O during acceleration to 3000 rpm. The analytical ultracentrifuge was started after 1 h of equilibration at 20 °C, with an acceleration rate of 600 rpm per minute. Data acquisition was carried out using an advanced Rayleigh interference optics (AIDA) developed by Nanolytics (Schilling and Krause 2015). In addition, the instrument was modified to allow data acquisition during the acceleration phase to directly observe the overlay process (Schneider et al. 2018). Differences between the custom-built analytical ultracentrifuge used in this study and standard commercial instruments have been documented in the literature (Bhattacharyya et al. 2006; Strauss et al. 2008; Walter et al. 2014; Schilling and Krause 2015; Walter and Peukert 2016; Pearson et al. 2018; Schneider and Cölfen 2018; Schneider et al. 2018).

Mathematical model

To describe the concentration gradient in the cell, we consider a section of an annulus with meniscus radius r_m (after the overlay) and bottom of the channel with the radius r_b. A schematic drawing of a channel can be found in Fig. 1. Assuming axial symmetry, the diffusion equation for the concentration c of the solvent is written in the radial coordinate r as

$$\frac{\partial^2 c}{\partial r^2} + \frac{1}{r}\frac{\partial c}{\partial r} = \frac{1}{D}\frac{\partial c}{\partial t}, \tag{1}$$

supplemented by the reflecting (zero current) boundary conditions

$$\frac{\partial c}{\partial r} = 0 \qquad \text{at } r = \{r_m, r_b\}, \tag{2}$$

and an initial condition after a disturbance free overlay

$$c(r, t=0) = F(r) = \begin{cases} c_i & r_m \le r \le r_m + h \\ 0 & r_m + h < r < r_b \end{cases}, \tag{3}$$

with h being the thickness of the upper solvent layer and c_i being the concentration of the less dense solvent in the reservoir, in this case H_2O. The thickness h can be calculated based on the overlay volume and the geometric characteristics of the centerpiece. We solve Eq. (1) using an eigenfunction expansion

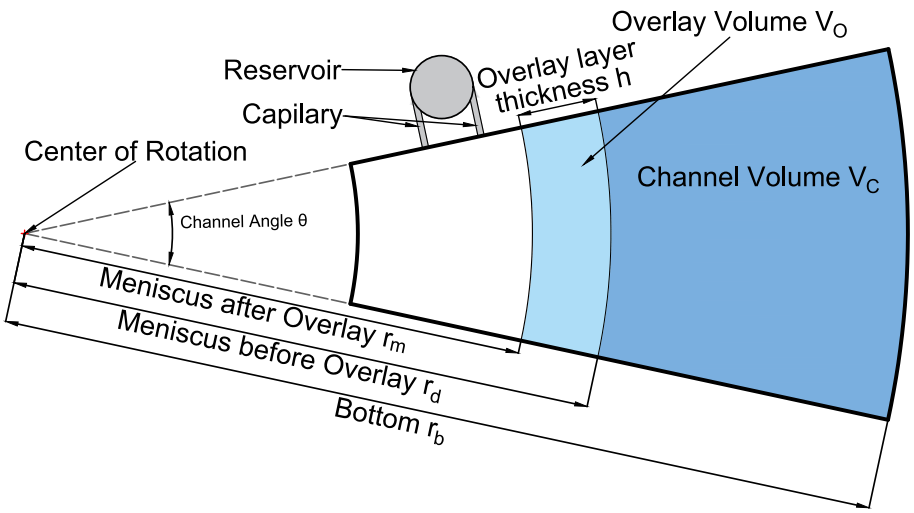

Fig. 1 Schematic drawing of a band-forming centerpiece channel with reservoir

$$c(r,t) = \sum_n a_n R(\beta_n, r)\exp\left(-D\beta_n^2 t\right), \tag{4}$$

where $R(\beta_n, r)$ is the solution of

$$\frac{\partial^2 R}{\partial r^2} + \frac{1}{r}\frac{\partial R}{\partial r} + \beta_n^2 R = 0, \tag{5}$$

which is the Bessel equation of zero order. The general solution of Eq. (5) is

$$R(\beta_n, r) = A_n J_0(\beta_n r) + B_n Y_0(\beta_n r), \tag{6}$$

where J_ν and Y_ν denote the Bessel functions of the first and second kind with ν specifying the order (Hahn and Özişik 2012).

Imposing the boundary conditions on Eq. (6) at r_m and r_b leads to $A_n = Y_1(\beta_n r_b)$, $B_n = J_1(\beta_n r_b)$, and the following transcendental equation for β_n

$$J_1\left(\beta_n r_m\right)Y_1\left(\beta_n r_b\right) - J_1\left(\beta_n r_b\right)Y_1\left(\beta_n r_m\right) = 0. \tag{7}$$

Finally, the expansion coefficients a_n can be found by expressing the initial condition, $F(r)$, in terms of the eigenfunctions $R(\beta_n, r)$. This leads to the following solution of the original problem

$$\begin{aligned} c(r,t) =& c_{\text{eq}} + \sum_n \frac{1}{N\left(\beta_n\right)} R\left(\beta_n, r\right)\exp\left(-D\beta_n^2 t\right) \\ & \int_{r_m}^{r_b} R\left(\beta_n, r'\right)F\left(r'\right)r'\mathrm{d}r' \end{aligned} \tag{8}$$

with the norm $N(\beta_n)$ given by

$$\frac{1}{N(\beta_n)} = \frac{\pi^2}{2}\frac{\beta_n^2 J_0'^2\left(\beta r_m\right)}{J_0'^2\left(\beta_n r_m\right) - J_0'^2\left(\beta r_b\right)}. \tag{9}$$

The first summand in (8), c_{eq}, is a constant term related to the first eigenvalue $\beta_0 = 0$. Physically, it corresponds to the equilibrium, uniform concentration of H_2O in the system, which can be calculated from the volumes loaded into the cell channel and reservoir.

With the initial condition given by Eq. (3) the integral in Eq. (8) takes the form

$$\begin{aligned} \int_{r_m}^{r_b} R(\beta, r')F(r')r'\mathrm{d}r' =& \left\{Y_1\left(\beta r_b\right)\left[r_d J_1\left(\beta r_d\right) - r_m J_1\left(\beta r_m\right)\right]\right. \\ & \left. + J_1\left(\beta r_b\right)\left[r_m Y_1\left(\beta r_m\right) - r_d Y_1\left(\beta r_d\right)\right]\right\}\frac{c_i}{\beta}. \end{aligned} \tag{10}$$

where $r_d = r_m + h$.

The calculation of the concentration profiles was carried out using the approach described above, with a C++ code developed by us to facilitate future integration into existing analysis software. The GNU scientific library was used to implement the Bessel functions. The eigenvalues were determined using a secant solver on the interval from 0.01 to 5000 and all found eigenvalues were used for the calculations.

For the diffusion of H_2O and D_2O, we assumed the mutual diffusion coefficient to be $D = 1.8 \times 10^{-5}$ cm^2/s as described in the Supporting Information (SI). The density and viscosity of the water and heavy water were taken from the parametrizations published in reference (Philo 2023). The channel was modeled as a section of a hollow cylinder with a height of 12 mm and an outer diameter of 7.166 cm and an inner diameter of 6.163 cm.

Thickness of the overlay layer

When the content of the reservoir is layered on top of the solution in the channel, the meniscus rises slightly to the position r_m. The thickness of this thin layer is a key parameter for the calculation of the concentration profiles of H_2O during the experiment. Previous studies considered only the effect of different overlay volumes on the thickness, without accounting for the channel angle or the volume within the channel V_C (Schneider et al. 2018). To determine the layer thickness, users had to follow the experimental protocol outlined by Schneider et al. (2018) This protocol required recording scans during the acceleration phase, which was not feasible without modified hardware and software.

Alternatively, the overlay thickness, h, can be calculated from a simple geometrical consideration, using the experimentally observed meniscus position, r_m, the channel angle (in radians), θ, channel height, l, and the overlay volume, V_O, as

$$h(\theta, V_O, r_m) = \sqrt{r_m^2 + \frac{2}{\theta l}V_O} - r_m. \tag{11}$$

With the knowledge of the volume filled into the column V_C, the sector angle θ and overlaid volume V_O, the meniscus shift h can also be calculated as

$$h(r_b, \theta, V_C, V_O) = \sqrt{r_b^2 - \frac{2}{\theta l}V_C} - \sqrt{r_b^2 - \frac{2}{\theta l}\left(V_C + V_O\right)}. \tag{12}$$

It is important to note that V_C and V_O are the planned volumes —i.e., the intended amounts to be filled. However, due to practical uncertainties in experimental preparation (e.g., incomplete emptying of reservoirs, residual liquid in pipettes, or acceleration-related deviations), these volumes may not reflect the actual values. As these errors are not reliably quantifiable, calculations based on these volumes involve an unknown uncertainty. The benefit of Eq. (11) compared to Eq. (12) is that the uncertainty of the channel volume V_C is avoided in favor of the experimentally determined meniscus position. In addition, the meniscus position

is already needed for the analysis of the AUC data. While the combination of both equations allows the calculation of the overlay thickness and the channel angle, measuring the channel angle in the centerpiece provides more precise results. This further reduces the uncertainty of the calculated overlay thickness.

Results and discussion

Calculation of concentration gradients

We compare the analytical predictions of the concentration profiles based on Eq. (8) with the recorded Rayleigh-interference data for a 10 µL overlay volume. The comparison is presented in Figure 2.

The comparison between the analytical calculations and the measured experimental profiles shows good agreement at later times (teal, bright pink, light pink, dark purple, blue), but shows a deviation at early times. This is because the rate of acceleration during the initial stage is much lower than in typical AUC experiments. Consequently, the timing of the overlay is primarily speed-dependent (Schneider and Cölfen 2018; Schneider et al. 2018). The presented model assumes the overlay to occur instantaneously, at $t = 0$. However, in the experimental data, it took three minutes to reach the final speed. The speed profile of this experiment is provided in the supporting information, Fig. S1. This slow acceleration explains the deviation observed, particularly in the earliest scan (black line in Fig. 2). However, the high accuracy of prediction at later times validates the accuracy of the $t = 0$ overlay assumption for experiments with low acceleration.

Additionally, the observed meniscus is broader due to the low rotational speed and the associated lower centrifugal forces, which counteract surface tension to a lesser extent. This results in a stronger surface curvature, leading to a less defined meniscus. Consequently, this causes a broader concentration profile of H_2O at lower rotation speeds compared to the same setups at higher rotation speeds. This affects especially scans taken during acceleration compared to scans taken after the end of the acceleration phase. This contributes in Fig. 2 to the missing area between the simulation profile and the measured signal for the earliest scan (black). The broadening of the meniscus dependent on the rotational speed was previously observed by Schneider et al. (2018) Earlier attempts to model the concentration profiles struggled to accurately represent the geometry of the system (Schneider and Cölfen 2018). The method described here correctly accounts for the shape of the centerpiece, ensuring a precise description of the radial dilution effect observed in AUC experiments. The radial dilution results in a steeper concentration profile compared to models assuming rectangular geometry, as manifested by an extra drift term, $(D/r)(\partial c/\partial r)$ in the diffusion equation, Eq. (1), which is not present in its rectangular counterpart. The evolution of the concentration gradient over time can be calculated, as shown in Fig. 3. The concentration of H_2O after 6 h is still slightly higher at the meniscus compared to the bottom. This emphasizes the importance of accounting for the effect of the dynamic gradient on the solvent of a BFE.

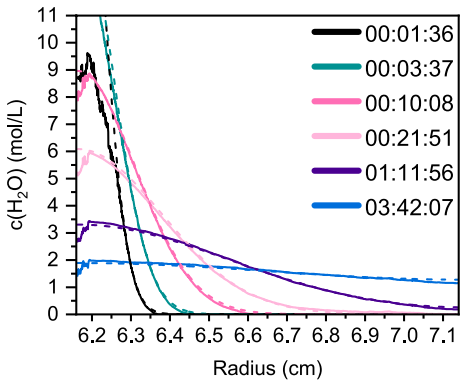

Fig. 2 The experimental interference (solid) and theoretical (dashed) profiles at different time points for the overlay of 10 µL H_2O onto D_2O

Given the concentration of H_2O, the density or viscosity of the H_2O–D_2O mixture can be calculated (Philo 2023). The general equation can be simplified for isotopic mixtures of water yielding a volume-fraction-weighted average for both density and viscosity (Steckel and Szapiro 1963; Philo 2023). By rewriting the volume fractions in terms of concentrations, the density can be expressed as

$$\rho(c_{H_2O}) = \rho_{D_2O} + \frac{\rho_{H_2O} - \rho_{D_2O}}{c_{self,H_2O}} c_{H_2O} \tag{13}$$

and the viscosity as

$$\eta(c_{H_2O}) = \eta_{D_2O} + \frac{\eta_{H_2O} - \eta_{D_2O}}{c_{self,H_2O}} c_{H_2O}, \tag{14}$$

where $c_{self,H_2O} = \rho_{H_2O}/M_{H_2O} = 55.56$ mol/L.

Impact of the channel angle

The channel angle plays a crucial role in several aspects of the analysis. It directly influences the radial dilution, introducing the dependence of volumes on radial positions. Additionally, the channel angle determines the thickness of the overlay layer, an essential parameter for calculating concentration profiles in Eq. (11).

The channel angle can be calculated based on the bottom radius, the meniscus position after the overlay, and the total volume, with the results shown in Fig. 4a. However,

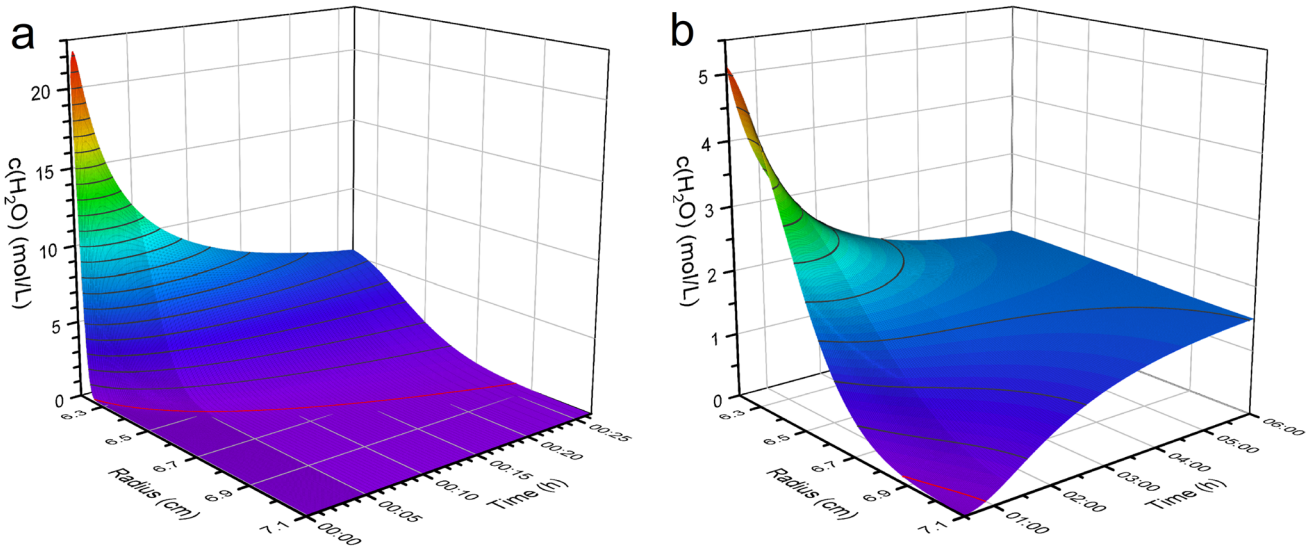

Fig. 3 Concentration profiles after the overlay of 10 µL H_2O onto D_2O. The profiles are shown shortly after the overlay (**a**) and at longer times (**b**). The red line marks the concentration of 0.1 mol/L H_2O

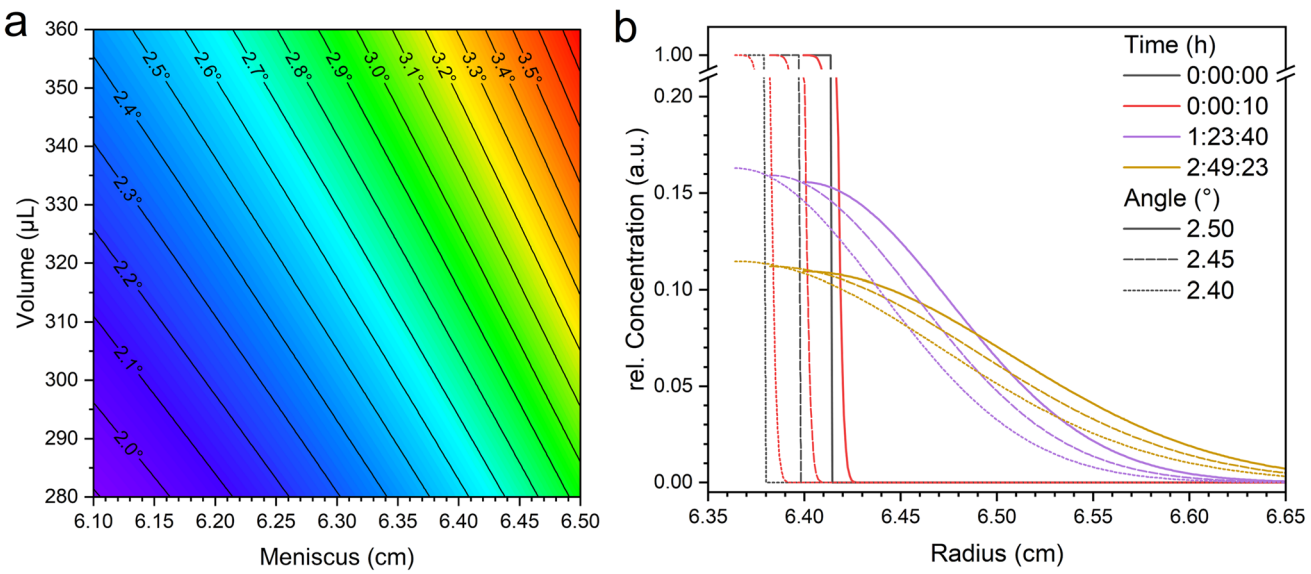

Fig. 4 Calculation of the channel angle (**a**) as a function of the volume and the meniscus position after overlay in a channel with a bottom of 7.166 cm. Comparison of the concentration profiles (**b**) for the same volume after overlay (const $V_C + V_O$) for 2.5° (solid), 2.45° (dashed) and 2.4° (dotted)

calculating the angle of the channel from experimental data requires more precise knowledge of the radial position of the meniscus and the volume than is currently achievable. The volume can deviate from the theoretical value due to the small portion of the overlaying solution that might remain in the reservoir or due to loading errors, which are hard to quantify in general. Typically, the uncertainty for the radial positions due to the optics is around 10 µm (Clodfelter and Schwartz 2017). However, the actual measurement error for the position of the meniscus is even greater, due to factors such as the curvature of the meniscus. Note that a meniscus shift of 50 µm results in a change in the channel angle of around 0.01°. Such a difference can significantly affect the concentration profiles when modeling the system, as demonstrated in Fig. 4. Although the volume after the overlay ($V_C + V_O$) remains constant across the different cases shown in the figure, the position of the meniscus shifts due to the variations in the channel angle. Fig. 4 demonstrates the importance of obtaining a reliable value for the channel angle to ensure precise calculations. The best way to

achieve this is through a direct measurement of the channel angle, which is sufficient for accurate predictions, as shown in Fig. 2, and is preferred over back-calculating the angle of the channel from the radial position of the meniscus and the overlay volume. The importance of measuring the channel angle is further underlined by the fact that centerpieces from different manufacturers can vary by as much as 1 degree in their channel angles. Failure to account for these variations when modeling individual channels would introduce significant errors.

Conclusion

In this study, we developed a mathematical model capable of predicting the diffusive mixing of two solution layers in a system with cylindrical geometry. This model closely matches experimental data of the overlay of H_2O onto D_2O, enabling, for the first time, an accurate description of solution density and viscosity throughout the entire experiment.

The key parameters in this model are the channel angle and the thickness of the overlay layer, both of which significantly influence the accuracy of the concentration profiles, as demonstrated by calculations for different channel angles. We also explored different approaches for estimating these parameters. Determining the overlay thickness or channel angle based solely on the position of the channel bottom and meniscus, along with the channel volume, was found to be insufficiently precise. Instead, we recommend a direct measurement of the channel angle before the experiment. This method eliminates the need for specialized hardware or software, making it accessible to researchers using standard laboratory equipment while ensuring accurate results.

The presented description for dynamic gradients, based on the diffusive mixing of two phases, is a significant step towards enabling researchers to analyze BFE. With this model, for the first time since the development of BFE 60 years ago, the dynamic gradients in density and viscosity can be accurately predicted. The model is also applicable to other solvents, provided that the diffusion coefficient, density, and viscosity of the solvent mixture are known.

Looking ahead, the current fitting algorithms in AUC analysis software will need to be adapted to accommodate position- and time-dependent variations in density and viscosity. With this model implemented, the analysis software should be capable of analyzing BFEs. Given the demonstrated accuracy for the prediction of gradients, it is plausible that Rayleigh interference detectors could be corrected for the signal caused by the dynamic gradient in the recorded data. This opens the opportunity to use Rayleigh interference detectors for BFEs of samples that are not detectable with UV/Visible detectors

Supplementary Information The online version contains supplementary material available at https://doi.org/10.1007/s00249-025-01759-7.

Acknowledgements The authors thank Helmut Cölfen, who passed away way too early, for his passion, kindness and supervision.

Research reported in this publication was supported by the National Institute of General Medical Sciences of the National Institutes of Health under award number R01GM120600 (to BD, EB). This work used Jetstream2 at Indiana University through allocation MCB070038 (to BD) from the Advanced Cyberinfrastructure Coordination Ecosystem: Services & Support (ACCESS) program, which is supported by U.S. National Science Foundation grants #2138259, #2138286, #2138307, #2137603, and #2138296.

LD is grateful to the Studienstiftung des Deutschen Volkes for a PhD fellowship.

Data availability All figure data and the raw interference data from the AUC experiment are available on Zenodo (https://doi.org/10.5281/zenodo.15601163).

References

Bhattacharyya SK, Maciejewska P, Börger L et al (2006) Development of a fast fiber based UV-Vis multiwavelength detector for an ultracentrifuge. Progress Colloid Polym Sci 131:9–22. https://doi.org/10.1007/2882_002

Börger L, Cölfen H, Antonietti M (2000) Synthetic boundary crystallization ultracentrifugation: a new method for the observation of nucleation and growth of inorganic colloids and the determination of stabilizer efficiencies. Colloids Surf A 163(1):29–38. https://doi.org/10.1016/S0927-7757(99)00427-6

Chaton CT, Herr AB (2015) Elucidating complicated assembling systems in biology using size-and-shape analysis of sedimentation velocity data. Methods Enzymol 562:187–204. https://doi.org/10.1016/BS.MIE.2015.04.004

Chou CY, Hsieh YH, Chang GG (2011) Applications of analytical ultracentrifugation to protein size-and-shape distribution and structure-and-function analyses. Methods 54:76–82. https://doi.org/10.1016/j.ymeth.2010.11.002

Clodfelter D, Schwartz C (2017) Linearity of BSA using absorbance & interference optics. https://www.beckman.de/resources/reading-material/application-notes/linearity-of-bsa-using-absorbance-interference-optics

Cölfen H (2023) Analytical ultracentrifugation in colloid and polymer science: new possibilities and perspectives after 100 years. Colloid Polym Sci 301(7):821–849. https://doi.org/10.1007/S00396-023-05130-0

Demeler B, Gorbet GE (2016) Analytical ultracentrifugation data analysis with UltraScan-III. In: Analytical ultracentrifugation. Springer Japan, Tokyo, p 119–143, https://doi.org/10.1007/978-4-431-55985-6_8

Diaz L, Peyrot C, Wilkinson KJ (2015) Characterization of polymeric nanomaterials using analytical ultracentrifugation. Environ Sci Technol 49(12):7302–7309. https://doi.org/10.1021/ACS.EST.5B00243

Edwards GB, Muthurajan UM, Bowerman S et al (2020) Analytical ultracentrifugation (auc): an overview of the application of fluorescence and absorbance auc to the study of biological macromolecules. Curr Protoc Mol Biol 133:e131. https://doi.org/10.1002/CPMB.131

Goertz V, Dingenouts N, Nirschl H (2009) Comparison of nanometric particle size distributions as determined by SAXS, TEM and analytical ultracentrifuge. Part Part Syst Character 26(1–2):17–24. https://doi.org/10.1002/PPSC.200800002

González-Rubio G, Hilbert H, Rosenberg R et al (2021) Simple determination of gold nanocrystal dimensions by analytical ultracentrifugation via surface ligand-solvent density matching. Nanomaterials 11:1427. https://doi.org/10.3390/NANO11061427

Hahn DW, Özişik MN (2012) Heat Conduction, Wiley, https://doi.org/10.1002/9781118411285

Henrickson A, Kulkarni JA, Zaifman J et al (2021) Density matching multi-wavelength analytical ultracentrifugation to measure drug loading of lipid nanoparticle formulations. ACS Nano 15(3):5068–5076. https://doi.org/10.1021/acsnano.0c10069

Karabudak E, Brookes E, Lesnyak V et al (2016) Simultaneous identification of spectral properties and sizes of multiple particles in solution with subnanometer resolution. Angew Chem Int Ed 55:11770–11774. https://doi.org/10.1002/anie.201603844

Khasa H, Kilby G, Chen X et al (2021) Analytical band centrifugation for the separation and quantification of empty and full AAV particles. Mol Therapy Methods Clin Dev 21:585–591. https://doi.org/10.1016/J.OMTM.2021.04.008

Lopez PC, Uttinger MJ, Traoré NE et al (2022) Multidimensional characterization of noble metal alloy nanoparticles by multi-wavelength analytical ultracentrifugation. Nanoscale 14:12928–12939. https://doi.org/10.1039/D2NR02633C

MacGregor IK, Anderson AL, Laue TM (2004) Fluorescence detection for the XLI analytical ultracentrifuge. Biophys Chem 108(1–3):165–185. https://doi.org/10.1016/J.BPC.2003.10.018

Mächtle W (1992) Determination of highly resolved particle size distributions in the submicron range by ultracentrifugation. Makromol Chem Macromol Symp 61(1):131–142. https://doi.org/10.1002/MASY.19920610111

Mächtle W (1999) High-resolution, submicron particle size distribution analysis using gravitational-sweep sedimentation. Biophys J 76(2):1080–1091. https://doi.org/10.1016/S0006-3495(99)77273-5

Maruno T, Usami K, Ishii K et al (2021) Comprehensive size distribution and composition analysis of adeno-associated virus vector by multiwavelength sedimentation velocity analytical ultracentrifugation. J Pharm Sci 110:3375–3384. https://doi.org/10.1016/J.XPHS.2021.06.031

Maruno T, Ishii K, Torisu T et al (2023) Size distribution analysis of the adeno-associated virus vector by the c(s) analysis of band sedimentation analytical ultracentrifugation with multiwavelength detection. J Pharm Sci 112(4):937–946. https://doi.org/10.1016/J.XPHS.2022.10.023

Mittal V, Völkel A, Cölfen H (2010) Analytical ultracentrifugation of model nanoparticles: comparison of different analysis methods. Macromol Biosci 10(7):754–762. https://doi.org/10.1002/MABI.200900446

Pearson J, Walter J, Peukert W et al (2018) Advanced multiwavelength detection in analytical ultracentrifugation. Anal Chem 90(2):1280–1291. https://doi.org/10.1021/acs.analchem.7b04056

Philo JS (2023) SEDNTERP: a calculation and database utility to aid interpretation of analytical ultracentrifugation and light scattering data. Eur Biophys J 52:233–266. https://doi.org/10.1007/s00249-023-01629-0

Planken KL, Cölfen H (2010) Analytical ultracentrifugation of colloids. Nanoscale 2(10):1849–1869. https://doi.org/10.1039/C0NR00215A

Ranasinghe M, Fogg JM, Catanese DJ et al (2023) Suitability of double-stranded dna as a molecular standard for the validation of analytical ultracentrifugation instruments. Eur Biophys J 52:267–280. https://doi.org/10.1007/S00249-023-01671-Y

Savelyev A, Brookes EH, Henrickson A et al (2023) A new UltraScan module for the characterization and quantification of analytical buoyant density equilibrium experiments to determine AAV capsid loading. Eur Biophys J 52(4–5):311–320. https://doi.org/10.1007/S00249-023-01641-4/FIGURES/7

Schilling K, Krause F (2015) Analysis of antibody aggregate content at extremely high concentrations using sedimentation velocity with a novel interference optics. PLoS One 10(3):e0120820. https://doi.org/10.1371/JOURNAL.PONE.0120820

Schneider CM, Cölfen H (2018) Analytical band centrifugation revisited. Eur Biophys J 47(7):799–807. https://doi.org/10.1007/s00249-018-1315-1

Schneider CM, Cölfen H (2019) High-resolution analysis of small silver clusters by analytical ultracentrifugation. J Phys Chem Lett 10(21):6558–6564. https://doi.org/10.1021/acs.jpclett.9b02755

Schneider CM, Cölfen H (2020) Formation of nanoclusters in gold nucleation. Curr Comput-Aided Drug Des 10(5):382. https://doi.org/10.3390/cryst10050382

Schneider CM, Haffke D, Cölfen H (2018) Band sedimentation experiment in analytical ultracentrifugation revisited. Anal Chem 90(18):10659–10663. https://doi.org/10.1021/acs.analchem.8b02768

Schuck P (2000) Size-distribution analysis of macromolecules by sedimentation velocity ultracentrifugation and Lamm equation modeling. Biophys J 78(3):1606–1619. https://doi.org/10.1016/S0006-3495(00)76713-0

Steckel F, Szapiro S (1963) Physical properties of heavy oxygen water. part 1. -density and thermal expansion. Trans Faraday Soc 59:331–343

Sternisha SM, Wilson AD, Bouda E et al (2023) Optimizing high-throughput viral vector characterization with density gradient equilibrium analytical ultracentrifugation. Eur Biophys J 52:387–392. https://doi.org/10.1007/S00249-023-01654-Z

Strauss HM, Karabudak E, Bhattacharyya S et al (2008) Performance of a fast fiber based UV/Vis multiwavelength detector for the analytical ultracentrifuge. Colloid Polym Sci 286(2):121–128. https://doi.org/10.1007/S00396-007-1815-5

Thajudeen T, Walter J, Srikantharajah R et al (2017) Determination of the length and diameter of nanorods by a combination of analytical ultracentrifugation and scanning mobility particle sizer. Nanoscale Horizons 2:253–260. https://doi.org/10.1039/C7NH00050B

Urban MJ, Holder IT, Schmid M et al (2016) Shape analysis of dna-au hybrid particles by analytical ultracentrifugation. ACS Nano 10:7418–7427. https://doi.org/10.1021/ACSNANO.6B01377

Uttinger MJ, Boldt S, Wawra SE et al (2020) New prospects for particle characterization using analytical centrifugation with sector-shaped centerpieces. Part Part Syst Character. https://doi.org/10.1002/PPSC.202000108

Vinograd J, Bruner R (1966a) Band centrifugation of macromolecules in self-generating density gradients. II. Sedimentation and diffusion of macromolecules in bands. Biopolymers 4(2):131–156. https://doi.org/10.1002/bip.1966.360040202

Vinograd J, Bruner R (1966b) Band centrifugation of macromolecules in self-generating density gradients. III. Conditions for convection-free band sedimentation. Biopolymers 4(2):157–170. https://doi.org/10.1002/bip.1966.360040203

Vinograd J, Bruner R, Kent R et al (1963) Band-centrifugation of macromolecules and viruses in self-generating density gradients. Proc Natl Acad Sci 49:902–910. https://doi.org/10.1073/pnas.49.6.902

Völkle CM, Gebauer D, Cölfen H (2015) High-resolution insights into the early stages of silver nucleation and growth. Faraday Discuss 179:59–77. https://doi.org/10.1039/C4FD00269E

Walter J, Löhr K, Karabudak E et al (2014) Multidimensional analysis of nanoparticles with highly disperse properties using multiwavelength analytical ultracentrifugation. ACS Nano 8(9):8871–8886. https://doi.org/10.1021/NN503205K

Walter J, Peukert W (2016) Dynamic range multiwavelength particle characterization using analytical ultracentrifugation. Nanoscale 8(14):7484–7495. https://doi.org/10.1039/C5NR08547K. https://pubs.rsc.org/en/content/articlehtml/2016/nr/c5nr08547k, https://pubs.rsc.org/en/content/articlelanding/2016/nr/c5nr08547k

Walter J, Gorbet G, Akdas T et al (2017) 2d analysis of polydisperse core-shell nanoparticles using analytical ultracentrifugation. Analyst 142:206–217. https://doi.org/10.1039/C6AN02236G

Wawra SE, Pflug L, Thajudeen T et al (2018) Determination of the two-dimensional distributions of gold nanorods by multiwavelength analytical ultracentrifugation. Nat Commun. https://doi.org/10.1038/S41467-018-07366-9

Wawra SE, Onishchukov G, Maranska M et al (2019) A multiwavelength emission detector for analytical ultracentrifugation. Nanoscale Adv 1(11):4422–4432. https://doi.org/10.1039/C9NA00487D

Wawra S, Kessler S, Egel A et al (2023) Hydrodynamic characterization of a vesicular stomatitis virus-based oncolytic virus using analytical ultracentrifugation. Eur Biophys J 52:379–386. https://doi.org/10.1007/S00249-023-01649-W

Xu X, Cölfen H (2021) Ultracentrifugation techniques for the ordering of nanoparticles. Nanomaterials 11(2):333. https://doi.org/10.3390/NANO11020333

Zhao H, Sousa AA, Schuck P (2024) Flotation coefficient distributions of lipid nanoparticles by sedimentation velocity analytical ultracentrifugation. ACS Nano 18:18663–18672. https://doi.org/10.1021/ACSNANO.4C05322